

Article

Influence of Bilayer Thickness on Mechanical and Tribological Properties of (Ti-Al)N/MoN Nanostructured Hard Coatings Deposited by Cathodic Arc Ion Plating

Muhammad I. Yousaf¹, Tushagu Abudouwufu^{2,3}, Bing Yang⁴, Alexander Tolstoguzov^{3,5,6}  and Dejun Fu^{2,3,7,*}

¹ Department of Applied Sciences, National Textile University, Faisalabad 37610, Pakistan; imran@ntu.edu.pk

² Key Laboratory of Artificial Micro- and Nanomaterials of Ministry of Education and Hubei Nuclear Solid Physics Key Laboratory, School of Physics and Technology, Wuhan University, Wuhan 430072, China; t2848077245@sina.com

³ Innovation Center of Tsinghua University Research Institute, Zhuhai 519000, China

⁴ School of Power & Mechanical Engineering, Wuhan University, Wuhan 430072, China; toyangbing@whu.edu.cn

⁵ Department of Space Technologies, Utkin Ryazan State Radio Engineering University, Gagarin Str. 59/1, 390005 Ryazan, Russia

⁶ Centre for Physics and Technological Research (CeFITec), Universidade Nova de Lisboa, 2829-516 Caparica, Portugal

⁷ Wuhan University Shenzhen Research Institute, 6 Yuexin 2nd Rd., Shenzhen 518057, China

* Correspondence: djfu@whu.edu.cn; Tel.: +86-276-875-3587

Abstract: Deposition of (Ti-Al)N/MoN multilayered coatings was carried out through a cathodic ion-plating system in an argon and then nitrogen atmosphere. Bilayer thickness (Λ) of all the samples were achieved, from 22 to 104 nm, by organizing substrate holder rotational speed (SRS). To obtain the optimum properties of the (Ti-Al)N/MoN coatings, the Ti and Al ratio was maintained at a level of 1:1. X-ray diffraction (XRD), high-resolution transmission electron microscopy (HRTEM), X-ray photoelectron spectroscopy (XPS), and Raman spectroscopy were utilized to analyze the crystal structure and morphology of the coatings. Mechanical and tribological properties were examined by nanohardness and atomic force microscopy (AFM). The preferred orientation of the (Ti-Al)N/MoN nanoscale multilayer films was TiAlN (200) and MoN (200), which had face centered cubic (fcc) and hexagonal structures, respectively. The hardness increased with the decrease in Λ (104 nm to 26 nm), and then it increased. The highest hardness of 37 GPa was revealed at $\Lambda = 26$ nm, whereas the least wear rate of $8.09 \times 10^{-7} \text{ mm}^3/\text{N.m}$ was attained at $\Lambda = 22$ nm. Wear rate, roughness, and coefficient of friction were decreased with decreasing bilayer period. EDS results showed that Al and Ti contents were almost the same in all samples, as per design of the experiment.

Keywords: (Ti-Al)N/MoN; multilayer nanocomposite; cathodic arc ion-plating; mechanical and tribological properties



Citation: Yousaf, M.I.; Abudouwufu, T.; Yang, B.; Tolstoguzov, A.; Fu, D. Influence of Bilayer Thickness on Mechanical and Tribological Properties of (Ti-Al)N/MoN Nanostructured Hard Coatings Deposited by Cathodic Arc Ion Plating. *Coatings* **2023**, *13*, 1654. <https://doi.org/10.3390/coatings13091654>

Academic Editor: Alberto Palmero

Received: 22 August 2023

Revised: 12 September 2023

Accepted: 14 September 2023

Published: 21 September 2023



Copyright: © 2023 by the authors. Licensee MDPI, Basel, Switzerland. This article is an open access article distributed under the terms and conditions of the Creative Commons Attribution (CC BY) license (<https://creativecommons.org/licenses/by/4.0/>).

1. Introduction

Cathodic arc ion plating technology was developed to supply ions that can assist in film formation, as well as become incorporated in the growing film. This technique is significantly different from others. Some of its characteristic features are as follows: (I) a significant proportion of the evaporated material is ionized; (II) the material plasma is produced by one or more arc spots; (III) the ions occur in multiple charge states; and (IV) the ions hold very high kinetic energies, i.e., 10–100 eV. These characteristics of this technique result in deposits that are of superior quality in comparison with those from other physical vapor deposition processes. Some of these advantages are as follows: (I) high deposition rates for metals, alloys and compounds with excellent coating uniformity; (II) good quality films over a broad range of deposition environments, e.g., stoichiometric reacted films with

enhanced adhesion and film density can be obtained over a wide range of reactive gas pressures and evaporation rates; (III) facilitation of reaction of compound films; (IV) low substrate temperature; and (V) confinement of alloy composition from source to deposit.

TiAlN coatings have been extensively used for engineering applications, e.g., cutting gears, dies, and wear. Compared to TiN coatings, they are better than TiN coatings in terms of hardness, wear resistance, oxidation control, and thermal stability [1–4] due to the proliferation of hardness and the alteration in micro stress brought on by lattice mismatch at the c-TiN and c-AlN contact [5,6]. However, it is imperative to further increase the hardness and wear properties of TiAlN films, given the advancement of engineering technologies, especially in numerical control cutting and high-speed cutting technology.

The crystalline nature and the biological, mechanical, and thermal properties of $Ti_{1-x}Al_xN$ coatings are greatly contingent on their alignments. The structure changes from a single-phase cubic composition to a mixed cubic-NaCl and wurtzite-ZnS (w) composition, and, finally, to a single-phase wurtzite structure when the Al concentration for $Ti_{1-x}Al_xN$ coatings increases [7,8] up to 70 at. % Al assimilation into the fcc. A TiN matrix is theoretically possible at the hexagonally close-packed (hcp) AlN phase, with merged Ti and a dual-phase structure with the fcc $Ti_{1-x}Al_xN$ phase all formed during the deposition process [9,10]. Such microstructure changes have a substantial influence on the coating properties that follow. Thus, aluminum content can significantly affect the coatings' tribological, mechanical, and structural characteristics. Therefore, an optimized Al concentration can be used to achieve the best Ti-Al-N coating properties. This is the fundamental idea driving all our group to work on $Ti_{(1-x)}Al_xN/MoN$ multilayer coatings. Due to the superior mechanical properties of the $Ti_{1-x}Al_xN$ coating at this ratio, the ratio of Ti to Al in the current study of nanoscale multilayered coatings has been kept close to 1:1 [11,12]. The Ti:Al ratio has an impact on $Ti_{1-x}Al_xN$ -based nanoscale multilayered coatings, changing the lattice parameter and elastic modulus [13,14]. The field of strain due to elastic moduli and change in lattice parameters between two layers is connected to the mechanical properties of the nanoscale multilayered coatings [15,16]. In contrast, because of the high cutting force, the temperature of the tool will rise undesirably and induces the wear process [17,18]. Friction force also can be abridged by adapting the chemical composition of the following elements by means of incorporating oxides emollients, such as in Ti, V, W, and Mo, known as oxides, which belong to the set called Magnéli phases. These elements' oxides exhibit obvious shear planes because of the precise positioning of their oxygen atoms, and, especially at higher temperatures, its lamellar structure also exhibits lubricating properties. In the literature, we can find three different ways to blend Mo with Ti-Al.

1. A multilayer structure encompassing TiAlN with Mo as a sublayer [19].
2. A multilayer structure tranquil of TiAlN and MoN/Mo₂N [20,21].
3. Coatings made of multiple $(TiAl)_{1-x}Mo_xN$ components and different molybdenum concentrations [22].

As the number of published research works related to $Ti_{(1-x)}Al_xN/MoN$ coatings and their relative (mechanical and thermal) properties are still rare, there seems to be no clear analysis or discussion related to this subject, especially with the 50:50 ratio of Ti and Al. With this Ti and Al concentration, a multilayer coating is expected to demonstrate high hardness and improved tribological presentation in the applications, especially in cutting discrete materials like Inconel 718 and TiAl6V4 alloys, which has a higher wear rate. By using Mo and Ti cathodes while altering the substrate's speed, multilayer $Ti_{0.50}Al_{0.50}N/MoN$ coatings are created in the current work, which is followed by a thorough analysis of their mechanical and tribological characteristics.

2. Materials and Methods

By using cathodic arc ion plating, $Ti_{0.50}Al_{0.50}N/MoN$ coatings were applied to polished Si (100) and cemented carbides. $Ti_{0.50}Al_{0.50}$ and Mo were selected as targets. Figure 1 displays the schematic diagram of the cathodic arc ion plating chamber. The chamber had

a volume of $54 \times 29.5 \times 39.5 \text{ cm}^3$, and there were 22.5 cm between the sample and the source. The chamber was evacuated to a base pressure of $3.4 \times 10^3 \text{ Pa}$ before the deposition. The substrates were cleaned with acetone and ultrasonically disinfected in a hot alkaline bath for 15 min and washed with deionized water. For 30 min, they were subjected to bombardment with Ar^+ and N_2 (at equal flow rates of 150 sccm) at a bias voltage of around 600 V with an 80% duty cycle. Complete deposition specifications are described in Table 1. An AFM (Shimadzu SPM-9500J3, Kyoto, Japan) was used on measuring area of $5 \times 5 \mu\text{m}^2$ with a tapping mode to examine the surface topography. Sirion FEG scanning electron microscopy (SEM) with an EDAX Genesis 7000 EDS was used to examine the topographical morphology and elemental composition. The crystal structure of the $\text{Ti}_{0.50}\text{Al}_{0.50}\text{N}/\text{MoN}$ coatings was examined using X-ray diffraction (XRD, D8 advanced) and Cu K radiation. The findings of the selected area electron diffraction (SAED) and bilayer period thickness measurements were evaluated using SEM, TEM (JEOL JEM 2010-HT, Tokyo, Japan), and HRTEM methods. An Escalab 250 Xi spectrometer from Thermo Scientific (Waltham, MA, USA) was used to calibrate X-ray photoelectron spectra (XPS). Utilizing a Renishaw RM-1000 confocal micro-Raman spectrometer driven by an Ar-ion laser at 488 nm, a point investigation of the film's phonon scattering was completed. Hardness and elastic modulus were measured using nano-indentation in constant stiffness measurement (CSM) mode with G200-Agilent Technologies, Santa Clara, CA, USA. The resolution of the displacement system and loading system were 0.04 nm and 50 nN, respectively. Indentation with a three-sided Berkovich shape and a tip radius of 60 nm was used, and the indentation depth was set at 500 nm. Six indentations were recorded for each sample. At 30 °C and 70% relative humidity in ambient air, the MS-T3000 ball-on-disk tester was used to measure the friction coefficient and wear rate. The counterpart was a Si_3N_4 ball with a diameter of 3 mm, a surface roughness R_a of 0.02 mm, and a hardness of 1600 HV50 g. A 5 N force was applied. The friction coefficients were recorded throughout the test, which was conducted sliding at 0.02 m/s for 60 min. At normal and higher temperatures, this material can observe coating tribo-chemical reactions without obviously plasticizing while avoiding additional chemical reactions. On an HH-3000 scratch tester, scratch tests were measured using a gradual rise of the standard load between 0 and 100 N, with a loading rate of 100 N per minute and a speed of 5 mm per minute. To study wear tacks, a Talysurf profilometer was used.

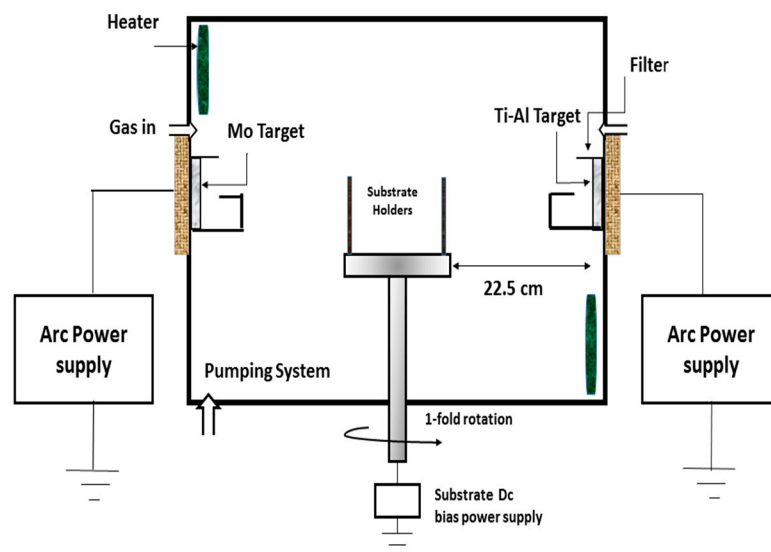


Figure 1. Experimental setup of the deposition system.

Table 1. Experimental description.

Deposition Parameters	
Base pressure (Pa)	3.4×10^{-3}
Cathode targets	Ti _{0.50} Al _{0.50} and Mo
Ar ⁺ bombard for cleaning	−600 V bias voltage with 80% duty cycle for 30 min
Source to substrate distance (cm)	22.5
Substrate bias voltage (−V)	150
Substrate temperature (°C)	325
Cathodic arc current (A)	60 for TiAl and 80 for Mo targets
Reactive gas	N ₂
Reactive gas pressure (Pa)	2.5
Substrate holder rotation speed (rpm)	1, 2, 3, 4, 5
Deposition time (minutes)	30
Interlayer(s)	Mo (−200 V Time = 8 min, P = 3.1×10^{-2} Pa, current = 80 A)
Rotational mode	1-Fold rotation

3. Results and Discussion

Individual X-ray diffraction patterns are shown in Figure 2. A multilayer film on Si (100) substrates composed of Ti_{0.50}Al_{0.50}N/MoN was deposited with varying bilayer periods. Only two phases are perceived: the δ -MoN phase and the TiAlN phase. The TiAlN patterns show preferred orientation along (200). The TiAlN alloy peaks are at 43° and at 62°, somewhat shifted towards higher angles corresponding to TiN (Fm-3 m space group, PDF-65-0970). The drop in crystalline constraints proves the swapping of Ti³⁺ by relatively smaller Al³⁺ ions and stress between the border line of MoN and TiAlN [23,24]. The peaks demonstrated at 2 θ (200) and (220) show face-centered cubic (fcc) structure of Al and Ti, which is also noticed in other studies [25–28]. The MoN peak displayed at 36.0° corresponds to extended hexagonal MoN (PDF-89-5024) [29]. According to the Debye–Scherrer formula, the widened sharp apex at 42.9° discloses a crystallite size of ~7.4 nm of TiAlN, and the peak of MoN at 48.3° divulges a crystallite size of ~7.0 nm in the case of the sample with a bilayer period of 104 nm. The peak (200) TiAlN's "d-planar" distance is 2.12, while the peak (200) MoN's is 2.48. The XRD results show that the TiAlN layers' particle sizes may be the cause of the phase advancement rather than the bilayer composition. It is noticeable that, as the bilayer period decreases, the reflection peak at 43° becomes sharper and higher in intensity, which shows that, because of the interface blocking, the average grain size decreases with decreasing period thickness [30].

For the samples put on Si substrates, Table 2 shows the elemental concentration assessed by the EDS method. Each sample's data were gathered at several locations, and the average was calculated over 5–7 measurements. Nearly all the samples have comparable TiAlN constituent elements, with a Ti: Al ratio of Ti_{0.515}Al_{0.485}N). The Ti:Al ratio is 1.03:0.97, which is slightly different from a premeditated value of 1:1. The presence of N in the MoN and TiAlN sublayers, as well as Mo in the interlayer, complicates the calculation of the Mo:N ratio in the sublayers.

The deposits on Si (100) substrates with different bilayer concentrations are evaluated by XPS spectra and as shown in Figure 3, the values of the binding energies are adjusted in relation to the C1s level at 284.6 eV. For fitting spectra, Gaussian–Lorentzian function was used. With the help of XPS spectra, we can obtain vast data related to the chemical assembly and bonding situations. The samples had apparently been contaminated with surface oxide because they had been exposed to air before the XPS measurement.

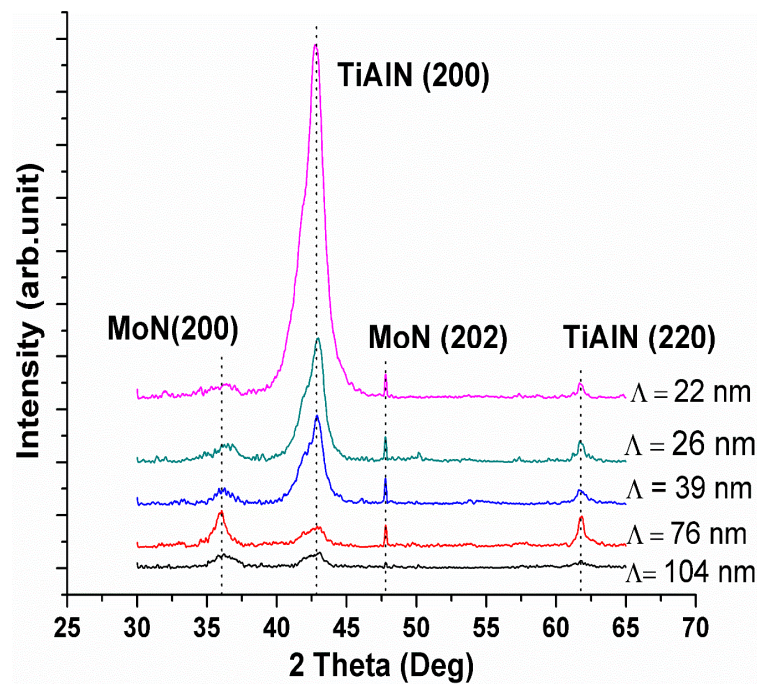


Figure 2. XRD patterns of (Ti-Al)N/MoN multilayer coatings.

Table 2. Elemental composition, grain size, thickness, of (Ti-Al)N/MoN nanomultilayers.

Λ (nm)	Element Composition [at%]				Thickness (Ti-Al)N/MoN (μm)	Grain Size TiAlN (nm)	Grain Size MoN (nm)
	Ti K	Al K	Mo L	N K			
104	17.49	15.54	43.25	23.72	1.33 ± 0.04	7.42 ± 0.2	7.08 ± 0.3
76	13.59	12.91	40.45	33.05	1.69 ± 0.02	6.91 ± 0.1	10 ± 0.4
39	16.82	15.91	43.21	24.06	1.91 ± 0.02	6.45 ± 0.2	8.60 ± 0.3
26	14.97	15.70	33.46	35.87	1.95 ± 0.04	6.77 ± 0.1	5.80 ± 0.3
22	12.67	11.38	37.82	38.12	2.91 ± 0.03	6.06 ± 0.1	4.17 ± 0.2
(Ti-Al)N	25.89	25.15	-	48.97	1.26 ± 0.03	5.48 ± 0.1	-
MoN	-	-	59.02	40.98	1.61 ± 0.04	-	14.59 ± 0.2

The films were also exposed to Ar^+ during XPS measurements for a few minutes in order to remove contaminants like carbon [31]. For the Ti 2p spectra exhibit at binding energies, there are two distinctive peaks of 455 (TiN peak) and 457.2 eV (TiNO peak, suggesting moderate surface oxidation) originally located at 454.95 and 456.5 eV, respectively. Chemical variations in the TiN film's core levels relative to the Ti element throughout the nitridation process are evidence of the charge transfer from titanium to nitrogen [32,33]. The 2p spectra of Al can be deconvoluted into two peaks, AlN and Al_2O_3 , which are located at 73.3 and 74.8 eV, respectively. The broader peak at 74.7 eV of a sample having $\Lambda = 26$ nm clearly shows that there exists AlN and Al_2O_3 . The spectra show that AlN is composed stoichiometrically and suggest that the Al atoms appear to be bound. The Ti 2p and Al 2p spectra closely match those from an earlier study [34]. The N1s spectra can be deconvoluted into three peaks, Mo ($3p_{3/2}$)N, TiAlN, and MoN, at 394.1, 396.2, and 397.1 eV, respectively. No chemical shift is observed, but FWHM variation could be discerned because XPS is a very sensitive technique, and the penetration depth is about 5 nm. Mo 3d can be deconvoluted into two peaks, MoN and MoO_2 , at 227.9 and 228.6 eV [35].

Figure 4 shows composite Raman spectra of the multilayer $\text{Ti}_{0.50}\text{Al}_{0.50}\text{N}/\text{MoN}$ structure on a stainless-steel substrate. The spectrum shows three bands centered at 200, 380, and 590 cm^{-1} . These bands are created by acoustic transitions in the $150\text{--}400 \text{ cm}^{-1}$ range and optical modes in the $450\text{--}650 \text{ cm}^{-1}$ range (LA and TA) (LO and TO) [36]. Each ion is located at an inversion symmetry location in an ideal fcc crystal structure (O_h symmetry),

which prevents the first order permitted Raman active phonon vibration [37]. In a cathodic arc ion plating system, many microscopic defects can arise, for example, nitrogen ion site vacancies that are lighter can exist and the presence of heavy metal ions.

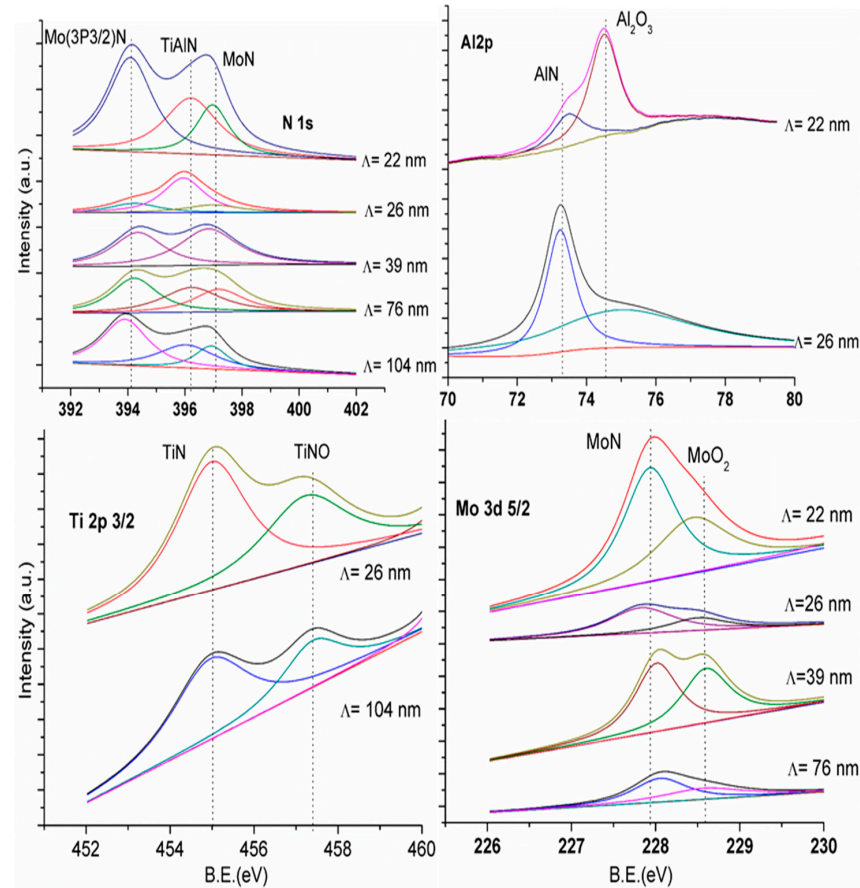


Figure 3. XPS spectra of $\text{Ti}_{0.5}\text{Al}_{0.5}\text{N}/\text{MoN}$ coatings.

The shifts of some atomic neighbors have non-zero first-order polarizability derivative, and these flaws reduce effective symmetry. Thus, the existence of impurities or flaws in the crystal is indicated by the Raman spectra of a perturbed crystal. The scattering phenomena in the acoustic range is due to titanium and molybdenum vibrations, and N ion vibrations caused scattering in the optical range [38,39]. In Figure 4, higher frequencies are used as the broadband associated with the optical band changes, and, by incorporating Al into the TiN matrix, the spectral density between the acoustic and optical modes increases. Between the acoustic and optical modes, the spectral density rises. This phenomenon is possibly due to the incorporation of defects because of the nonstoichiometric state of the coatings [11]. The first order Raman spectrum of TiN changes to higher frequencies, according to prior research, as the nitrogen deficiency increases [37,40].

In the acoustic transition band, we observed three peaks at 180 , 215 , and 370 cm^{-1} , referred to as the MoN, TiN, and AlN phases [11–41]. In the optical region of modes, we observed one main peak at 580 cm^{-1} , referred to as the TiN phase, as compared with previous studies [11,41].

Figure 5a,b show continuous columnar structures with an average coating thickness of $1.26\text{ }\mu\text{m}$ of as-deposited $\text{Ti}_{0.5}\text{Al}_{0.5}\text{N}$ monolayer and $1.61\text{ }\mu\text{m}$ thickness of as-deposited MoN monolayer. Figure 5c shows a surface morphology of a multilayer $\text{Ti}_{0.5}\text{Al}_{0.5}\text{N}/\text{MoN}$ coating with $\Lambda = 22\text{ nm}$. All films contained spherical micro-droplets, which is a shortcoming of the cathodic arc. Droplets arise when low melting point materials, such as aluminum, evaporate in an arc (Ti, Al, and Mo). It is believed that, due to fast evaporation, too many atoms which are not ionized yet reach the surface of substrate. These additional neutral

atoms might interact during battle and form macro-particles. Previous studies confirmed the form of the micro-droplet is spherical for Al content ≤ 0.60 . Beyond this, it becomes flat [27], which is also proven in this study.

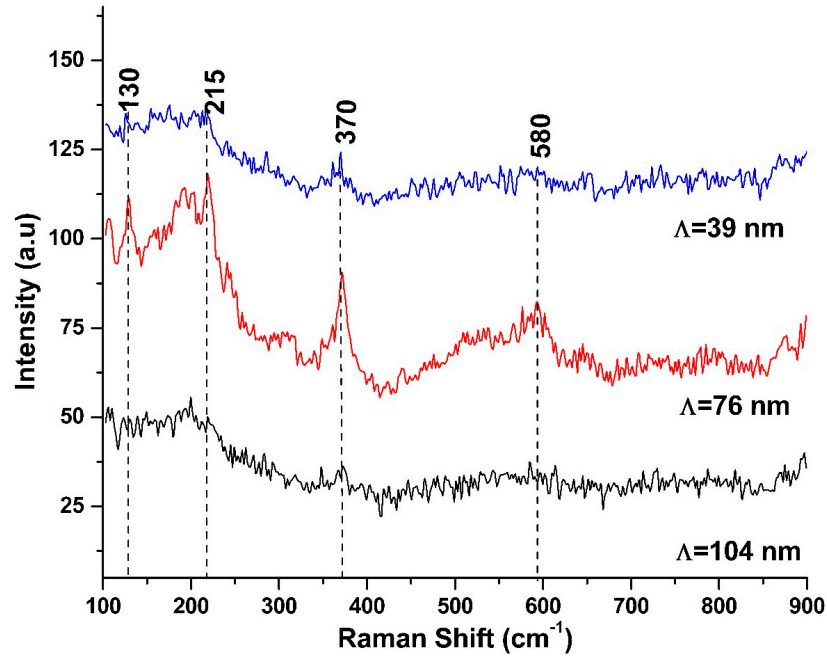


Figure 4. Raman spectra of nanomultilayer samples.

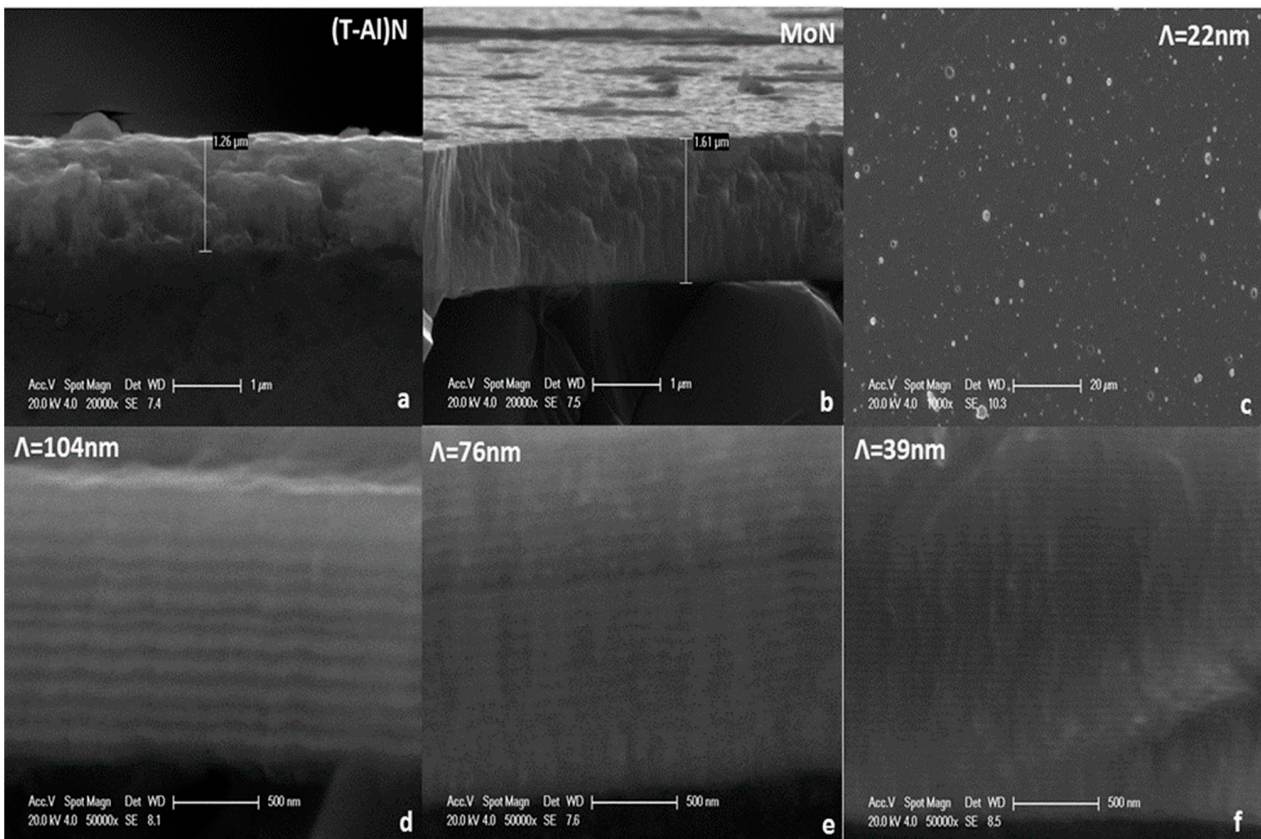


Figure 5. SEM surface morphology micrograph: (a) (Ti-Al)N monolayer (b) MoN monolayer (c) $\Lambda = 22$ nm sample and SEM cross-sectional image (d) $\Lambda = 104$ nm sample (e) $\Lambda = 76$ nm sample (f) $\Lambda = 39$ nm sample.

SEM images of cross sectional (Ti-Al)N/MoN multilayer, thin films on Si (100) substrate are shown in Figure 5d–f, and one can see different multilayer structures very well. The morphology, thickness of layers, and multilayered formation calculated through SEM images are further verified from TEM and HR-TEM images, which are presented in Table 2.

In Figure 6, these images on Si (100) substrates show the surface morphology and roughness of the coating that were examined using AFM. A $5 \times 5 \text{ m}^2$ measurement area was chosen at random from the coating positions. The surface profile is used to establish the morphology of column growth indications and to present trends on the mechanical strength of the coatings. In general, plain view topography consists of hemispherical, rounded hillock mounds. These mounds appear to be related to the columns' growth, reduction in size, and agglomeration as the bilayer period shortens. Higher roughness is obtained on samples with a bilayer period of 104 nm, and the other shows a continuing decrease with the bilayer period. Similar behavior was reported in a previous study [42]. Table 3 also shows that, as the bilayer period decreases, the roughness decreases from 15.6 to 8.5 nm.

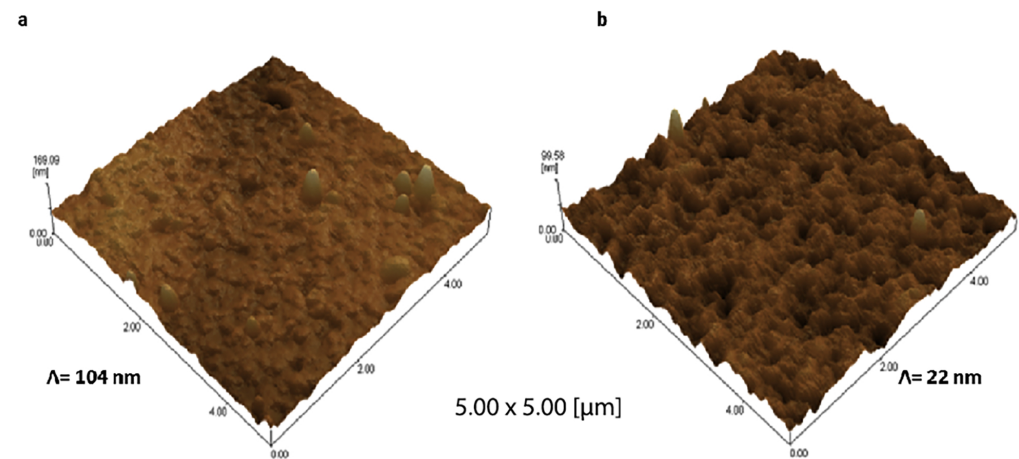


Figure 6. Three-dimensional AFM images of (Ti-Al)N/MoN coatings. (a) $\Lambda = 104 \text{ nm}$; (b) $\Lambda = 22 \text{ nm}$.

Table 3. Tribological and mechanical properties of (Ti-Al)N/MoN multilayer thin films.

Λ (nm)	Roughness (RMS) nm	Friction Coef.	Hardness (GPa)	Elastic Modulus (GPa)	H/E*	H ³ /E* ² (GPa)	Wear Rate (mm ³ /N·m)	Critical Load (N)
104	15.60	0.52 ± 0.03	33 ± 1.5	575 ± 25	0.055	0.101	1.56 × 10 ⁻⁶	78 ± 5 (L _{C1})
76	13.73	0.50 ± 0.04	32 ± 0.5	500 ± 30	0.061	0.122	2.10 × 10 ⁻⁶	87 ± 3 (L _{C1})
39	23.01	0.42 ± 0.02	34 ± 0.5	510 ± 30	0.064	0.141	1.29 × 10 ⁻⁶	71 ± 4 (L _{C1})
26	17.9	0.39 ± 0.02	37 ± 0.5	540 ± 20	0.066	0.162	1.45 × 10 ⁻⁶	75 ± 5 (L _{C1})
22	8.52	0.38 ± 0.07	32 ± 2	600 ± 20	0.051	0.085	8.09 × 10 ⁻⁷	91 ± 3 (L _{C1})
(Ti-Al)N	27.78	0.53 ± 0.04	30 ± 2	470 ± 20	0.061	0.114	1.56 × 10 ⁻⁵	75 ± 3 (L _{C1})
MoN	7.50	0.38 ± 0.02	31 ± 1	550 ± 15	0.054	0.092	5.36 × 10 ⁻⁷	>100 (L _{C1})

Whereas E* is effective Young's modulus. One of the principal factors that governs film durability, and one of the vital properties of thin films, is the adhesion of the substrate, i.e., the film substrate interfacial bonding strength. To determine the critical load, the coatings on the cemented carbide substrates underwent a scratch test. The results are shown in Table 3. An optical microscope was also used to confirm these findings. L_{C1} is used as a load for first critical cracking and scratching. Due to spallation at the groove side, the coatings become crashed, and L_{C2} was used as a load. The high plasticity at higher Λ [43,44] and before the deposition is related to the increase in L_C with the bilayer period. Mo bombardment for several minutes at high voltage also enhances the coating's adhesion quality [45]. Because of the high energy metal ions, bombardment etches the

substrate material and modifies the surface. Additionally, this process creates nucleation sites and facilitates the subsequent coating growth. Because of its hardness and the thermal expansion coefficient between the TiAlN/MoN multilayer and substrate, molybdenum is anticipated to increase film adherence [46].

HRTEM of a cross sectional $\text{Ti}_{0.50}\text{Al}_{0.50}\text{N}/\text{MoN}$ nanocomposite multilayer coating having $\Lambda = 22$ nm is shown in Figure 7c. The figure depicts a nanomultilayer architecture with bright and dark layers that alternate. Observable diffraction spots showing MoN (200), TiAlN (200), and TiAlN (220) are visible in Figure 7d, the selected area electron diffraction (SAED) image with $\Lambda = 22$ nm from TEM, which is in excellent accord with the XRD findings. HRTEM-EDS microanalysis (Figure 7b) of dark MoN layers clearly shows the presence of Mo in the majority, and Figure 7a shows that Ti and Al are the major elements in the bright layers.

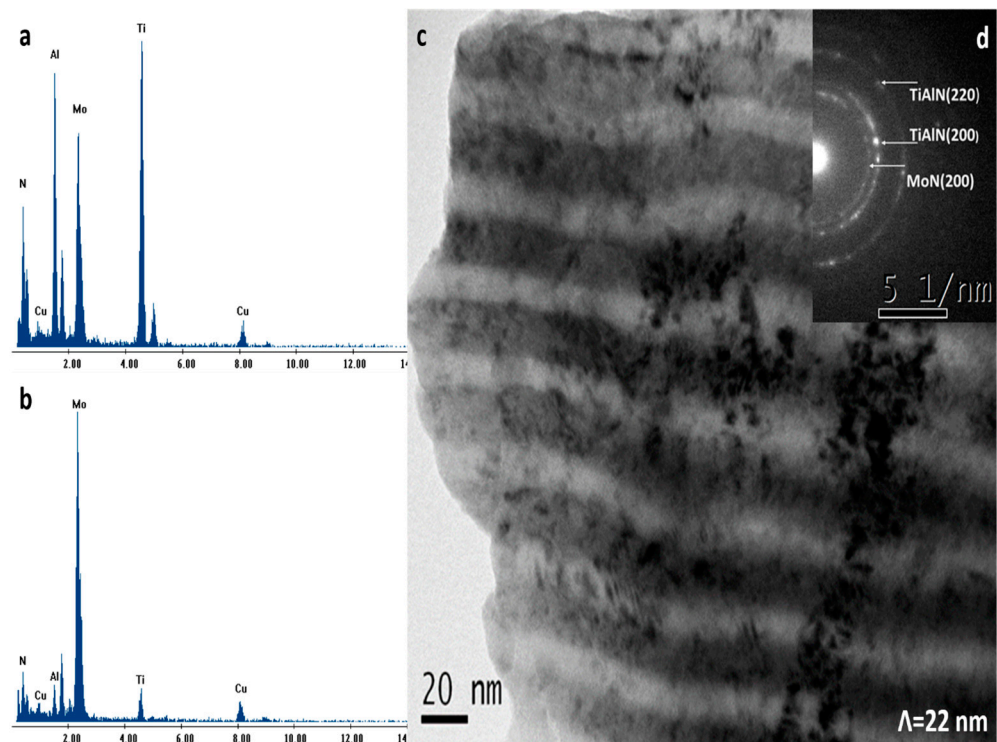


Figure 7. TEM EDS analysis: (a) bright layers; (b) dark layers; (c) TEM cross-sectional image of a sample having $\Lambda = 22$ nm; (d) SAED of a sample having $\Lambda = 22$ nm.

Figure 8a,b, with a bilayer period of 26 nm, show a bright TiAlN sublayer with an interplanar distance of 0.211 nm and the dark MoN interplanar space of 0.246 nm. It can be concluded that both MoN and TiAlN phases in the coating are of nanocrystalline sizes, and black MoN layers alternate with bright TiAlN layers. MoN and TiAlN have grains that are less than 10 nm in the current study, and J. Musil [47] lists four different types of nanostructures that can affect how hard the nanocomposite coatings are: (1) Nanoscale period bilayers (a mixture of nano-grains with various crystallographic orientations and/or phases), (2) columnar nanostructure, (3) nano-grains surrounded by thin (1 to 2 ML) tissue phase, and (4) nano-grains. This means that the bilayer period also affects the hardness. The CSM mode was employed to examine the coating's elastic modulus and nanohardness on tungsten carbide substrates. The as-measured elastic modulus and hardness against 500 nm indentation depth are listed in Table 3 and in Figure 9, with a Poisson's ratio of 0.18. In the 30–80 nm depth scale, hardness primarily increases with indentation depth; at greater depths, the hardness fluctuates with depth. When indenting at relatively shallow depths (≤ 20 nm), the measured hardness values are low due to the film's roughness or the Berkovich indenter tip's bluntness. Samples with a thickness of 26 nm show a

maximum hardness of 37 GPa. According to Table 3, all multilayered thin films are harder than monolayers. We are familiar with that phenomenon. In many multilayered nanoscale coating systems, the hardness rises to apparent saturation before falling as the Λ decreases. In this study, the hardness ascended to 26 nm before falling. This phenomenon causes the inhibition of a displacement sign activated by an image force that is depicted at the displacement near the $\text{Ti}_{0.50}\text{Al}_{0.50}\text{N}$ and MoN interlink, because of the difference in the elastic moduli in the $\text{Ti}_{0.50}\text{Al}_{0.50}\text{N}$ and MoN layers [48]. However, for small Λ , an increased interface width portion of individual layer thickness reduces the critical shear stress required to move a dislocation, decreasing the hardness of the nanoscale multilayered coating. The increase in hardness in the present coating can also be explained with the help of bonding characteristics. In AB compounds, the bulk modulus increases as the distance to the nearest neighbor decreases. Assuming that the increase in hardness is correlated with the increase in bulk modulus, the compound's increased hardness can be explained by a decrease in interatomic distance caused by an increase in the concentration of Al [25].

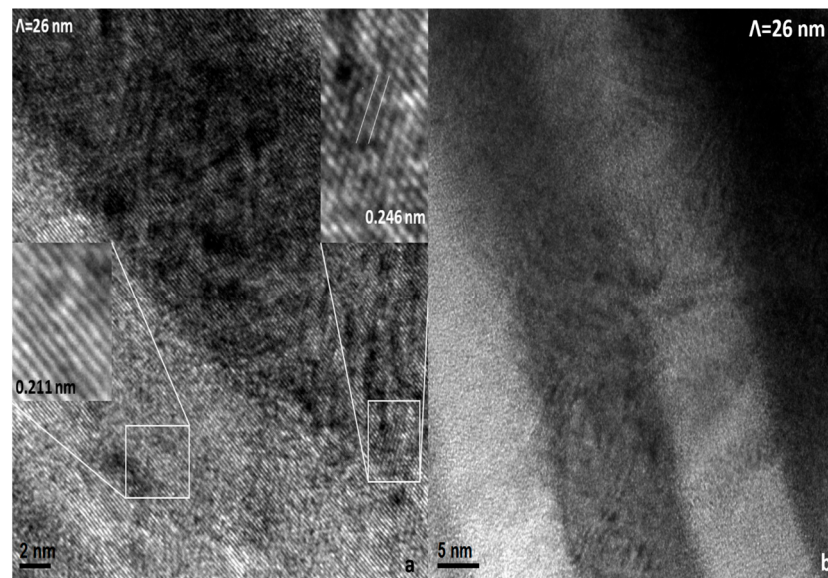


Figure 8. (a,b) HRTEM cross-sectional image of sample having bilayer period of 26 nm. The right inset shows interplanar distance of dark MoN layers, and the left inset shows interplanar distance of light (Ti-Al)N layers.

Moreover, there may be another explanation for the increase in hardness associated with the covalent energy in these coatings. In the formula $E_h = kd^{-22.5}$, (d) is the interatomic distance and (E_h) is the covalent band gap. Another factor that is equally as important as hardness is Young's modulus. It is appropriate to have a low modulus because it permits the given load to be dispersed over a large area. Table 3 displays the values of H/E^* and H^3/E^{*2} . It is challenging to find a straightforward correlation between the film's effective Young's modulus (E^*) and hardness (H). The combinations of a hard film's H and E have a significant impact on its mechanical behavior. However, by choosing both its chemical make-up and the deposition conditions that led to its creation, the correlation between H and E^* in the hard film can be managed [49,50]. These findings are quite consistent with earlier research [20,21].

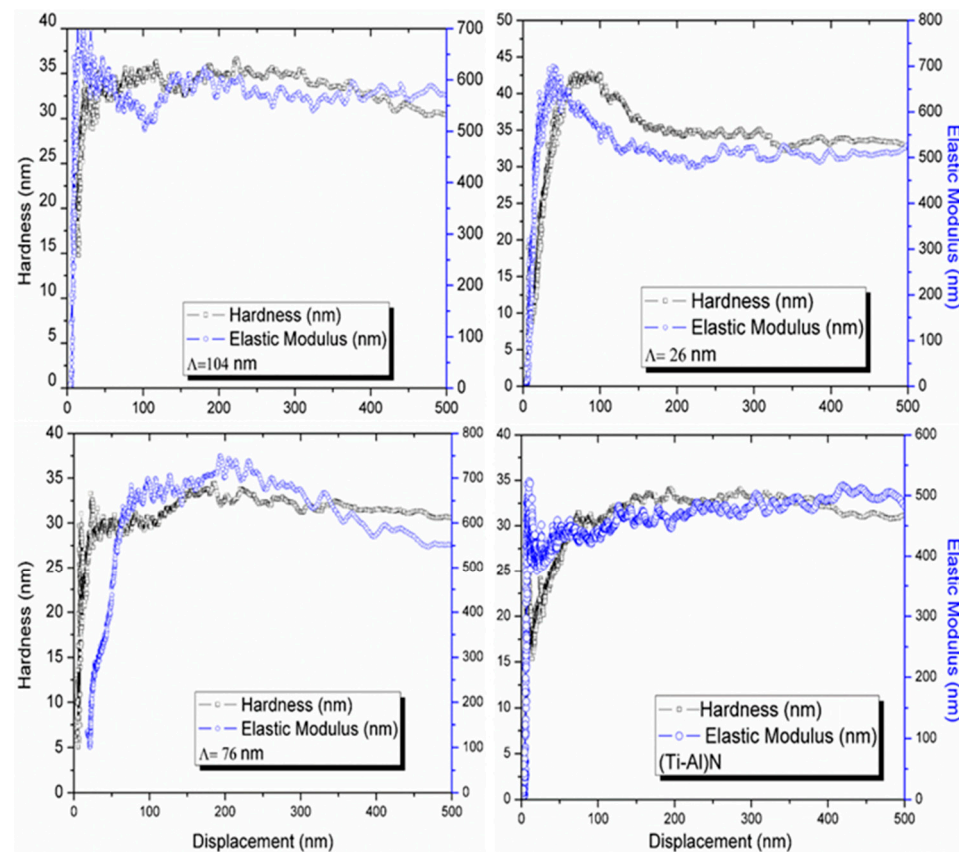


Figure 9. Nanohardness and Young's modulus as functions of displacement.

Friction coefficients of $\text{Ti}_{0.50}\text{Al}_{0.50}\text{N}/\text{MoN}$ coatings are in the range of 0.38–0.52 (Table 3). Molybdenum oxides, which are a byproduct of tribo-chemical oxidation, are responsible for these low friction coefficients. Other groups have also verified the self-lubrication of these oxides [51,52]. The production of these oxides is due to tribo-contact, which is mechanically and thermally caused by flash-type temperature pulses produced by deformation and shearing of micro-asperities during dry wear sliding. Other groups have observed similar low friction coefficient results because of the self-lubricating action when utilizing vanadium-containing TiAlN-based coatings [53–55]. These outcomes also outperform our previous studies, i.e., lower Al content and high Al content [20,21]. The better wear resistance with this Ti and Al concentration also matches very well with another previous study [46]. The dropping of friction forces and, thus, the dissipation of this reduced energy throughout the surface with the sliding contact, consequently, also reduces the wear rate of the studied coatings. As demonstrated in Figure 10, none of the coatings that were put to the test were entirely worn off throughout the test; in samples with bilayer periods of 22 nm $\text{Ti}_{0.50}\text{Al}_{0.50}\text{N}/\text{MoN}$, the most reliable wear mode is exhibited by the multilayer coating. According to all sample descriptions, there is no chipping or delamination of the coatings in Figure 10. Instead, defects can be seen as “droplets” that follow the path left by the sliding counter body and develop left-sunk fractures. For another possible explanation, the coating itself may also have exhibited brittle fractures. $\text{Ti}_{0.50}\text{Al}_{0.50}\text{N}/\text{MoN}$'s wear mechanism combines microgrooves, oxidation, and wear resistance. The calculations in this paper link with the recent investigations related to these materials [17,56]. Table 3 provides an overview of wear rate, friction coefficient, and surface roughness.

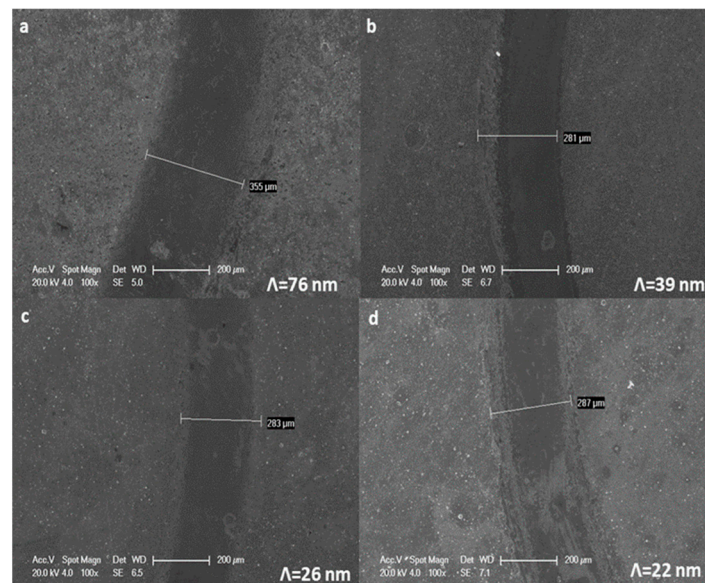


Figure 10. SEM morphology of the wear track of (Ti-Al)N/MoN coatings. (a) $\Lambda = 76$ nm sample, (b) $\Lambda = 39$ nm sample, (c) $\Lambda = 26$ nm sample, (d) $\Lambda = 22$ nm sample.

4. Conclusions

Cathodic arc ion plating was used to successfully lodge $\text{Ti}_{0.50}\text{Al}_{0.50}\text{N}/\text{MoN}$ nanomultilayer coatings. Rotation speed adjustments were used to organize the bilayer period Λ . Λ plays an important role in microstructure, mechanical, and tribological characteristics, as well as wear behavior in all the multilayer thin films. The TiAlN composition was essentially identical, with a Ti:Al ratio of $\text{Ti}_{0.50}\text{Al}_{0.50}\text{N}$. XRD patterns show that, as the bilayer period decreases, the reflection peaks at 43° become sharper and have higher intensities. From this result, we can imagine that the average size of the grain decreases with the reducing period thickness. Perhaps the producing interfaces are preventing the grain from progressing. The HRTEM, XRD, and SEM all agree on layer count, Λ , grain size, inter-planar spacing, and nanomultilayer structure. With increasing Λ up to 26 nm, the hardness and elastic modulus of the $\text{Ti}_{0.50}\text{Al}_{0.50}\text{N}/\text{MoN}$ multilayer structure improved and, thereafter, declined. Because the elastic moduli of the $\text{Ti}_{0.50}\text{Al}_{0.50}\text{N}$ and MoN layers vary, this phenomenon results in the inhibition of the displacement sign induced by an image force that appears at the displacement near the interlink between the two materials. $\text{Ti}_{0.50}\text{Al}_{0.50}\text{N}/\text{MoN}$ multilayer structures have better hardness and Young's moduli than their monolayer counterparts. In samples with a bilayer period of 22 nm, the most stable wear mode was confirmed, and wear rates were decreased by cutting the bilayer period. Comparing the $\text{Ti}_{0.50}\text{Al}_{0.50}\text{N}/\text{MoN}$ coating to other coatings with greater and lower Al content, the $\text{Ti}_{0.50}\text{Al}_{0.50}\text{N}/\text{MoN}$ coating has good tribological performances. In summary, the densified microstructure of $\text{Ti}_{0.50}\text{Al}_{0.50}\text{N}/\text{MoN}$ films, with the growth of fine grains and decreased surface roughness, were linked to their better mechanical characteristics with the decreasing the bilayer period, as demonstrated by measurements of nanoindentation in conjunction with AFM and cross-sectional SEM. $\text{Ti}_{0.50}\text{Al}_{0.50}\text{N}/\text{MoN}$ showed perfect tribological performances in comparison to coatings with greater and lower aluminum concentrations.

Author Contributions: Conceptualization: D.F. and B.Y.; investigation: M.I.Y.; visualization: T.A. and A.T.; formal analysis, D.F., B.Y., A.T. and T.A.; writing—original draft preparation: M.I.Y.; writing—review and editing: D.F., B.Y., A.T. and T.A.; funding acquisition: D.F., B.Y., A.T. and T.A. All authors have read and agreed to the published version of the manuscript.

Funding: This scientific work was supported by the National Natural Science Foundation of China under grant Nos. 12305328 and 12375285 and by the Shenzhen Municipal Committee on Science and Technology Innovation under grant No. JCYJ20220530140605011.

Institutional Review Board Statement: Not applicable.

Informed Consent Statement: Not applicable.

Data Availability Statement: Data sharing is not applicable to this article.

Conflicts of Interest: The authors declare no conflict of interest.

References

1. El-Hossary, F.M.; Abd El-Rahman, A.M.; Raaif, M.; Ghareeb, D.A. Properties of TiAlN Coating Deposited by MPIIID on TiN Substrates. *Appl. Phys. A Mater. Sci. Process.* **2016**, *122*, 242. [[CrossRef](#)]
2. Devia, D.M.; Restrepo-Parra, E.; Arango, P.J.; Tschiptschin, A.P.; Velez, J.M. TiAlN Coatings Deposited by Triode Magnetron Sputtering Varying the Bias Voltage. *Appl. Surf. Sci.* **2011**, *257*, 6181–6185. [[CrossRef](#)]
3. Endrino, J.L.; Fox-Rabinovich, G.S.; Escobar Galindo, R.; Kals, W.; Veldhuis, S.; Soriano, L.; Andersson, J.; Gutiérrez, A. Oxidation Post-Treatment of Hard AlTiN Coating for Machining of Hardened Steels. *Surf. Coat. Technol.* **2009**, *204*, 256–262. [[CrossRef](#)]
4. Fox-Rabinovich, G.S.; Endrino, J.L.; Beake, B.D.; Aguirre, M.H.; Veldhuis, S.C.; Quinto, D.T.; Bauer, C.E.; Kovalev, A.I.; Gray, A. Effect of Temperature of Annealing below 900 °C on Structure, Properties and Tool Life of an AlTiN Coating under Various Cutting Conditions. *Surf. Coat. Technol.* **2008**, *202*, 2985–2992. [[CrossRef](#)]
5. Mayrhofer, P.H.; Willmann, H.; Hultman, L.; Mitterer, C. Influence of Different Atmospheres on the Thermal Decomposition of Al-Cr-N Coatings. *J. Phys. D. Appl. Phys.* **2008**, *41*, 155316. [[CrossRef](#)]
6. Hasegawa, H.; Kimura, A.; Suzuki, T. Microhardness and Structural Analysis of (Ti,Al)N, (Ti,Cr)N, (Ti,Zr)N and (Ti,V)N Films. *J. Vac. Sci. Technol. A Vac. Surf. Films* **2000**, *18*, 1038–1040. [[CrossRef](#)]
7. Chawla, V.; Jayaganthan, R.; Chandra, R. Influence of Sputtering Pressure on the Structure and Mechanical Properties of Nanocomposite Ti-Si-N Thin Films. *J. Mater. Sci. Technol.* **2010**, *26*, 673–678. [[CrossRef](#)]
8. McIntyre, D.; Greene, J.E.; Håkansson, G.; Sundgren, J.E.; Münz, W.D. Oxidation of Metastable Single-Phase Polycrystalline Ti_{0.5}Al_{0.5}N Films: Kinetics and Mechanisms. *J. Appl. Phys.* **1990**, *67*, 1542–1553. [[CrossRef](#)]
9. Kimura, A.; Hasegawa, H.; Yamada, K.; Suzuki, T. Effects of Al Content on Hardness, Lattice Parameter and Microstructure of Ti_{1-x}Al_xN Films. *Surf. Coat. Technol.* **1999**, *120–121*, 438–441. [[CrossRef](#)]
10. Liu, Z.-J.; Shen, Y.G. Effects of Al Content on Grain Growth of Solid Solution (Ti,Al)N Films. *J. Vac. Sci. Technol. A Vac. Surf. Films* **2006**, *24*, 174–177. [[CrossRef](#)]
11. Kutschej, K.; Mayrhofer, P.H.; Kathrein, M.; Polcik, P.; Tessadri, R.; Mitterer, C. Structure, Mechanical and Tribological Properties of Sputtered Ti_{1-x}Al_xN Coatings with 0.5 ≤ x ≤ 0.75. *Surf. Coat. Technol.* **2005**, *200*, 2358–2365. [[CrossRef](#)]
12. PalDey, S.; Deevi, S.C. Single Layer and Multilayer Wear Resistant Coatings of (Ti,Al)N: A Review. *Mater. Sci. Eng. A* **2003**, *342*, 58–79. [[CrossRef](#)]
13. Yashar, P.C.; Sproul, W.D. Nanometer Scale Multilayered Hard Coatings. *Vacuum* **1999**, *55*, 179–190. [[CrossRef](#)]
14. Cheng, Y.H.; Tay, B.K.; Lau, S.P.; Shi, X. Influence of Substrate Bias on the Structure and Properties of (Ti, Al)N Films Deposited by Filtered Cathodic Vacuum Arc. *J. Vac. Sci. Technol. A Vac. Surf. Films* **2001**, *19*, 736–742. [[CrossRef](#)]
15. Rafaja, D.; Wüstefeld, C.; Baehtz, C.; Klemm, V.; Dopita, M.; Motylenko, M.; Michotte, C.; Kathrein, M. Effect of Internal Interfaces on Hardness and Thermal Stability of Nanocrystalline Ti_{0.5}Al_{0.5}N Coatings. *Metall. Mater. Trans. A Phys. Metall. Mater. Sci.* **2011**, *42*, 559–569. [[CrossRef](#)]
16. Shum, P.W.; Li, K.Y.; Zhou, Z.F.; Shen, Y.G. Structural and Mechanical Properties of Titanium-Aluminium-Nitride Films Deposited by Reactive Close-Field Unbalanced Magnetron Sputtering. *Surf. Coat. Technol.* **2004**, *185*, 245–253. [[CrossRef](#)]
17. Liu, A.; Deng, J.; Cui, H.; Chen, Y.; Zhao, J. Friction and Wear Properties of TiN, TiAlN, AlTiN and CrAlN PVD Nitride Coatings. *Int. J. Refract. Met. Hard Mater.* **2012**, *31*, 82–88. [[CrossRef](#)]
18. Arndt, M.; Kacsich, T. Performance of New AlTiN Coatings in Dry and High Speed Cutting. *Surf. Coat. Technol.* **2003**, *163*, 674–680. [[CrossRef](#)]
19. Tavares, C.J.; Vidrigo, C.; Rebouta, L.; Rivière, J.P.; Le Bourhis, E.; Denicot, M.F. Optimization and Thermal Stability of TiAlN/Mo Multilayers. *Surf. Coat. Technol.* **2005**, *200*, 288–292. [[CrossRef](#)]
20. Yousaf, M.I.; Pelenovich, V.O.; Yang, B.; Liu, C.S.; Fu, D.J. Effect of Bilayer Period on Structural and Mechanical Properties of Nanocomposite TiAlN/MoN Multilayer Films Synthesized by Cathodic Arc Ion-Plating. *Surf. Coat. Technol.* **2015**, *282*, 94–102. [[CrossRef](#)]
21. Yousaf, M.I.; Pelenovich, V.O.; Yang, B.; Liu, C.S.; Fu, D.J. Influence of Substrate Rotation Speed on the Structure and Mechanical Properties of Nanocrystalline AlTiN/MoN Coatings Synthesized by Cathodic Arc Ion-Plating. *Surf. Coat. Technol.* **2015**, *265*, 117–124. [[CrossRef](#)]
22. Tabakov, V.P.; Chikhranov, A.V. Influence of the Composition of Three-Element Nitride Coatings on the State and Wear of a Cutting Tool. *Russ. Eng. Res.* **2010**, *30*, 84–89. [[CrossRef](#)]
23. Bhadeshia, H.K.D.H. Developments in Martensitic and Bainitic Steels: Role of the Shape Deformation. *Mater. Sci. Eng. A* **2004**, *378*, 34–39. [[CrossRef](#)]
24. Riedl, H.; Koller, C.M.; Limbeck, A.; Kalaš, J.; Polcik, P.; Mayrhofer, P.H. Oxidation Behavior and Tribological Properties of Multilayered Ti-Al-N/Mo-Si-B Thin Films. *J. Vac. Sci. Technol. A Vac. Surf. Films* **2015**, *33*, 05E129. [[CrossRef](#)]

25. Zhou, M.; Makino, Y.; Nose, M.; Nogi, K. Phase Transition and Properties of Ti-Al-N Thin Films Prepared by r.f.-Plasma Assisted Magnetron Sputtering. *Thin Solid Films* **1999**, *339*, 203–208. [[CrossRef](#)]
26. Pemmasani, S.P.; Valleti, K.; Gundakaram, R.C.; Rajulapati, K.V.; Mantripragada, R.; Koppoju, S.; Joshi, S.V. Effect of Microstructure and Phase Constitution on Mechanical Properties of $Ti_{1-x}Al_xN$ Coatings. *Appl. Surf. Sci.* **2014**, *313*, 936–946. [[CrossRef](#)]
27. Tanaka, Y.; Gür, T.M.; Kelly, M.; Hagstrom, S.B.; Ikeda, T.; Wakihira, K.; Satoh, H. Properties of $(Ti_{1-x}Al_x)N$ Coatings for Cutting Tools Prepared by the Cathodic Arc Ion Plating Method. *J. Vac. Sci. Technol. A Vac. Surf. Films* **1992**, *10*, 1749–1756. [[CrossRef](#)]
28. Lu, J.H.; Chen, B.Y. Colored Hard Coatings with AlN–TiN Multilayer Structures. *J. Vac. Sci. Technol. A Vac. Surf. Films* **2014**, *32*, 02B106. [[CrossRef](#)]
29. Kazmanli, M.K.; Ürgen, M.; Cakir, A.F. Effect of Nitrogen Pressure, Bias Voltage and Substrate Temperature on the Phase Structure of Mo-N Coatings Produced by Cathodic Arc PVD. *Surf. Coat. Technol.* **2003**, *167*, 77–82. [[CrossRef](#)]
30. Ducros, C.; Benevent, V.; Sanchette, F. Deposition, Characterization and Machining Performance of Multilayer PVD Coatings on Cemented Carbide Cutting Tools. *Surf. Coat. Technol.* **2003**, *163–164*, 681–688. [[CrossRef](#)]
31. Greczynski, G.; Hultman, L. Self-Consistent Modelling of X-ray Photoelectron Spectra from Air-Exposed Polycrystalline TiN Thin Films. *Appl. Surf. Sci.* **2016**, *387*, 294–300. [[CrossRef](#)]
32. Prieto, P.; Kirby, R.E. X-ray Photoelectron Spectroscopy Study of the Difference between Reactively Evaporated and Direct Sputter-Deposited TiN Films and Their Oxidation Properties. *J. Vac. Sci. Technol. A Vac. Surf. Films* **1995**, *13*, 2819–2826. [[CrossRef](#)]
33. Shum, P.W.; Zhou, Z.F.; Li, K.Y.; Shen, Y.G. XPS, AFM and Nanoindentation Studies of $Ti_{1-x}Al_xN$ Films Synthesized by Reactive Unbalanced Magnetron Sputtering. *Mater. Sci. Eng. B Solid-State Mater. Adv. Technol.* **2003**, *100*, 204–213. [[CrossRef](#)]
34. Greczynski, G.; Petrov, I.; Greene, J.E.; Hultman, L. Al Capping Layers for Nondestructive X-ray Photoelectron Spectroscopy Analyses of Transition-Metal Nitride Thin Films. *J. Vac. Sci. Technol. A Vac. Surf. Films* **2015**, *33*, 05E101. [[CrossRef](#)]
35. Choi, J.G.; Thompson, L.T. XPS Study of As-Prepared and Reduced Molybdenum Oxides. *Appl. Surf. Sci.* **1996**, *93*, 143–149. [[CrossRef](#)]
36. Spengler, W.; Kaiser, R. First and Second Order Raman Scattering in Transition Metal Compounds. *Solid State Commun.* **1976**, *18*, 881–884. [[CrossRef](#)]
37. Spengler, W.; Kaiser, R.; Christensen, A.N.; Müller-Vogt, G. Raman Scattering, Superconductivity, and Phonon Density of States of Stoichiometric and Nonstoichiometric TiN. *Phys. Rev. B* **1978**, *17*, 1095–1101. [[CrossRef](#)]
38. Franck, M.; Celis, J.P. Microprobe Raman Spectroscopy of TiN Coatings Oxidized by Solar Beam Heat Treatment. *J. Mater. Res.* **1995**, *10*, 119–125. [[CrossRef](#)]
39. Bondarev, A.V.; Kiryukhantsev-Korneev, P.V.; Sheveyko, A.N.; Shtansky, D.V. Structure, Tribological and Electrochemical Properties of Low Friction TiAlSiCN/MoSeC Coatings. *Appl. Surf. Sci.* **2015**, *327*, 253–261. [[CrossRef](#)]
40. Soignard, E.; Shebanova, O.; McMillan, P.F. Compressibility Measurements and Phonon Spectra of Hexagonal Transition-Metal Nitrides at High Pressure: ϵ -TaN, δ -MoN, and Cr_2N . *Phys. Rev. B Condens. Matter Mater. Phys.* **2007**, *75*, 014104. [[CrossRef](#)]
41. Barshilia, H.C.; Rajam, K.S. Raman Spectroscopy Studies on the Thermal Stability of TiN, CrN, TiAlN Coatings and Nanolayered TiN/CrN, TiAlN/CrN Multilayer Coatings. *J. Mater. Res.* **2004**, *19*, 3196–3205. [[CrossRef](#)]
42. Huang, S.H.; Chen, S.F.; Kuo, Y.C.; Wang, C.J.; Lee, J.W.; Chan, Y.C.; Chen, H.W.; Duh, J.G.; Hsieh, T.E. Mechanical and Tribological Properties Evaluation of Cathodic Arc Deposited CrN/ZrN Multilayer Coatings. *Surf. Coat. Technol.* **2011**, *206*, 1744–1752. [[CrossRef](#)]
43. Settineri, L.; Levi, R. Surface Properties and Performance of Multilayer Coated Tools in Turning Inconel. *CIRP Ann. Manuf. Technol.* **2005**, *54*, 515–518. [[CrossRef](#)]
44. Valli, J.; Mäkelä, U.; Matthews, A.; Murawa, V. TiN Coating Adhesion Studies Using the Scratch Test Method. *J. Vac. Sci. Technol. A Vac. Surf. Films* **1985**, *3*, 2411–2414. [[CrossRef](#)]
45. Suzuki, T.; Huang, D.; Ikuhara, Y. Microstructures and Grain Boundaries of (Ti,Al)N Films. *Surf. Coat. Technol.* **1998**, *107*, 41–47. [[CrossRef](#)]
46. Lin, K.L.; Hwang, M.Y.; Wu, C.D. The Deposition and Wear Properties of Cathodic Arc Plasma Deposition TiAlN Deposits. *Mater. Chem. Phys.* **1996**, *46*, 77–83. [[CrossRef](#)]
47. Musil, J. Hard Nanocomposite Coatings: Thermal Stability, Oxidation Resistance and Toughness. *Surf. Coat. Technol.* **2012**, *207*, 50–65. [[CrossRef](#)]
48. Chu, X.; Barnett, S.A. Model of Superlattice Yield Stress and Hardness Enhancements. *J. Appl. Phys.* **1995**, *77*, 4403–4411. [[CrossRef](#)]
49. Mooser, E. Bonds and Bands in Semiconductors. *Cryst. Semicond. Mater. Devices* **1988**, *169*, 1–54. [[CrossRef](#)]
50. Musil, J.; Kunc, F.; Zeman, H.; Poláková, H. Relationships between Hardness, Young's Modulus and Elastic Recovery in Hard Nanocomposite Coatings. *Surf. Coat. Technol.* **2002**, *154*, 304–313. [[CrossRef](#)]
51. Gulbinski, W.; Suszko, T.; Sienicki, W.; Warcholiński, B. Tribological Properties of Silver-and Copper-Doped Transition Metal Oxide Coatings. *Wear* **2003**, *254*, 129–135. [[CrossRef](#)]
52. Suszko, T.; Gulbiński, W.; Jagielski, J. The Role of Surface Oxidation in Friction Processes on Molybdenum Nitride Thin Films. *Surf. Coat. Technol.* **2005**, *194*, 319–324. [[CrossRef](#)]
53. Kutschej, K.; Mayrhofer, P.H.; Kathrein, M.; Polcik, P.; Mitterer, C. Influence of Oxide Phase Formation on the Tribological Behaviour of Ti-Al-V-N Coatings. *Surf. Coat. Technol.* **2005**, *200*, 1731–1737. [[CrossRef](#)]

54. Pfeiler, M.; Kutschej, K.; Penoy, M.; Michotte, C.; Mitterer, C.; Kathrein, M. The Effect of Increasing V Content on Structure, Mechanical and Tribological Properties of Arc Evaporated Ti-Al-V-N Coatings. *Int. J. Refract. Met. Hard Mater.* **2009**, *27*, 502–506. [[CrossRef](#)]
55. Zhou, Z.; Rainforth, W.M.; Rodenburg, C.; Hyatt, N.C.; Lewis, D.B.; Hovsepian, P.E. Oxidation Behavior and Mechanisms of TiAlN/VN Coatings. *Metall. Mater. Trans. A Phys. Metall. Mater. Sci.* **2007**, *38*, 2464–2478. [[CrossRef](#)]
56. Ávila, R.F.; Mancosu, R.D.; Machado, A.R.; Vecchio, S.D.; da Silva, R.B.; Vieira, J.M. Comparative Analysis of Wear on PVD TiN and (Ti_{1-x}Al_x)N Coatings in Machining Process. *Wear* **2013**, *302*, 1192–1200. [[CrossRef](#)]

Disclaimer/Publisher’s Note: The statements, opinions and data contained in all publications are solely those of the individual author(s) and contributor(s) and not of MDPI and/or the editor(s). MDPI and/or the editor(s) disclaim responsibility for any injury to people or property resulting from any ideas, methods, instructions or products referred to in the content.